Climate Dynamics (2024) 62:895–910
https://doi.org/10.1007/s00382-023-06942-0

Distinctive characteristics and dynamics of the summer and autumn Indian ocean dipole events

Yuqi Tao[1] · Chunhua Qiu[1] · Wenxiu Zhong[2,3] · Guangli Zhang[1] · Lin Wang[1]

Received: 9 May 2023 / Accepted: 26 August 2023 / Published online: 13 September 2023

Abstract

The Indian Ocean Dipole (IOD) with worldwide socio-economic impacts has been presented to mature either in boreal summer or autumn, leading to the classification of summer IOD and autumn IOD. Investigating the climate dynamics to distinguish between these two types of IOD can improve our understanding and prediction of the surrounding weather and climate. This study demonstrates that the emergence of the summer IOD is mainly attributed to internal air-sea interactions in the western tropical Indian Ocean (WIO), while the autumn IOD is significantly related to ENSO development. For the summer IOD, broad-scaled warm sea surface temperature anomalies in the WIO are conducive to the enhancement of convective perturbations. Then local ocean–atmosphere feedback associated with changes in convection and surface heat flux into the upper ocean plays a key role in triggering the summer IOD. For the autumn IOD, strong easterly wind anomalies in the eastern Indian Ocean initiate oceanic Rossby waves and Bjerknes feedback, leading to the formation of both the western and eastern poles. It is recognized that these intensified easterly wind anomalies mostly benefit from ENSO variability. The distinctive features and air-sea interactions intrinsic to the summer IOD and the autumn IOD revealed in this study can further contribute to more credible predictive models of diverse IOD events.

Keywords Indian Ocean dipole · ENSO · Air-sea interactions · Oceanic dynamics

1 Introduction

The Indian Ocean Dipole (IOD) is one of the dominant coupled ocean–atmosphere modes in the tropical Indian Ocean (TIO) that is manifested in a zonal dipole pattern of sea surface temperature anomalies (SSTAs; Saji et al. 1999). The positive IOD (pIOD) is characterized by warm SSTAs in the western TIO (WIO) and surface cooling in the southeastern TIO (Saji et al. 1999; Webster et al. 1999). The occurrence of IOD exerts significant impacts on surrounding areas and leads to worldwide climate teleconnections via atmospheric bridges and oceanic pathways (Li and Mu 2001; Saji and Yamagata 2003). Therefore, it is necessary to comprehensively investigate the mechanisms responsible for IOD events.

IOD exhibits diverse temporal-spatial characteristics. Canonical IOD events are known to develop mostly in boreal summer and mature in the following autumn, presenting obvious seasonal phase-locking features (Saji et al. 1999; Webster et al. 1999). However, another type of IOD referred to as the unseasonable IOD, possesses an earlier onset and a shorter duration, mostly developing and maturing within the boreal summer (Du et al. 2013). Previous studies have suggested that both internal variability within the Indian Ocean and external forcing from other basins contribute to the diversity of IOD (Rao and Behera 2005; Terray et al. 2007; Hong et al. 2008c; Sun et al. 2015; Yang et al. 2015; Chen et al. 2016, 2021; Stuecker et al. 2017; Jiang et al. 2022; Jiang and Liu 2022; Ling et al. 2022; Zhang et al. 2022a). This implies that the evolution of IOD may be

✉ Chunhua Qiu
qiuchh3@mail.sysu.edu.cn

✉ Wenxiu Zhong
zhongwx9@mail.sysu.edu.cn

[1] School of Marine Sciences, Sun Yat-Sen University, Southern Marine Science and Engineering Guangdong Laboratory (Zhuhai), Zhuhai, China

[2] School of Atmospheric Sciences, Sun Yat-Sen University, Southern Marine Science and Engineering Guangdong Laboratory (Zhuhai), Zhuhai, China

[3] Guangdong Province Key Laboratory for Climate Change and Natural Disaster Studies, Sun Yat-Sen University, Guangzhou, Guangdong, China

affected by multiple air–sea coupling processes, complicating our understanding and prediction of diverse IOD events.

ENSO has been identified as a major external factor influencing IOD (Annamalai et al. 2003; Fischer et al. 2005; Cai et al. 2011b; Roxy et al. 2011; Guo et al. 2015; Fan et al. 2017; Liu et al. 2017; Stuecker et al. 2017). About 40% of IOD events occur simultaneously with ENSO (Hong et al. 2008c). During an El Niño event, the weakened Walker circulation results in easterly wind anomalies along the equatorial Indian Ocean (Ashok et al. 2003; Behera et al. 2006). These easterly winds can initiate positive Bjerknes feedback, energizing pIOD events (Wang and Wang 2014; Zhang et al. 2015; Liu et al. 2017). The upper-ocean thermal structure in the Indian Ocean can also be influenced by ENSO through Rossby waves (Xie et al. 2009, 2016) and Indonesian Throughflow (ITF; Annamalai et al. 2003; Song et al. 2007; Tozuka et al. 2007), creating favorable conditions for IOD occurrence. Therefore, ENSO can significantly affect IOD by regulating both atmospheric circulation and oceanic pathways. However, not all IOD events are associated with ENSO, and vice versa (Ashok et al. 2003; Fischer et al. 2005; Behera et al. 2006; Wang et al. 2016; Lu and Ren 2020; Zhang et al. 2020, 2022b; Jiang and Liu 2022; Song and Ren 2022). Some IOD events may be triggered by local air-sea interactions within the Indian Ocean, independent of ENSO (Rao and Behera 2005; Behera et al. 2006; Wang et al. 2016). The crucial role of internal variability in triggering IOD has also been highlighted by Luo et al. (2008), as well as the importance of the subtropical Indian Ocean Dipole (SIOD; Behera and Yamagata 2001) acting as a precursor for IOD occurring several months later (Terray et al. 2007). The subtropical high linked to the SIOD can promote easterly wind anomalies along the eastern TIO, initiating IOD even in the absence of ENSO (Feng et al. 2014; Zhang et al. 2018, 2020; Huang et al. 2021).

Previous studies have suggested that cold SSTAs in the eastern TIO (EIO) are key factors in the development of pIOD events (Webster et al. 1999; Luo et al. 2010; Yang et al. 2015). The intensity, onset time, and spatial distribution of easterly wind anomalies, which are related to the formation of the eastern pole of IOD events, have been extensively investigated (Du et al. 2013; Sun et al. 2014; Guo et al. 2015; Endo and Tozuka 2016; Zhang et al. 2019; Cai et al. 2021; Jiang et al. 2022). However, the SST distribution in the WIO also differs during the evolution of IOD and plays an important role in the diversity of IOD events (Schott et al. 2009; Du et al. 2020, 2023; Zhang et al. 2020). Therefore, understanding the dynamic processes responsible for the evolution of the western pole is also crucial for improving predictions of different types of IOD events. Additionally, the WIO is considered an important moisture source for the Indian summer monsoon, which strongly influences the IOD (Ashok et al. 2001). Different SST distributions in the WIO can induce distinct monsoonal rainfall patterns, which locally modify air-sea interactions in the Indian Ocean (Drbohlav et al. 2007; Hong et al. 2008a, b; Effy et al. 2020). Thus, further investigation of the atmospheric-oceanic dynamics responsible for the western pole of IOD can deepen our understanding of the diversity of IOD events.

Given the distinct temporal-spatial characteristics of autumn IOD and summer IOD (respectively referred to as the canonical IOD and the unseasonable IOD in previous studies), this study aims to further investigate the different ocean–atmosphere coupling processes responsible for the evolution of the eastern and western poles of these two types of IOD events. The remaining part of this paper is organized as follows. Section 2 presents the data and methods used in this study. In Sect. 3.1, the temporal-spatial characteristics of summer IOD and autumn IOD are described. In Sect. 3.2, we analyze the mixed layer heat budget to reveal the dynamics and thermodynamics that are responsible for the evolution of the eastern and western poles of these two types of IOD events. In Sect. 3.3, we highlight the distinctive linkages between ENSO and these two types of IOD events. The results have been summarized and discussed in Sect. 4.

2 Data and methods

2.1 Data

Monthly SST data on a horizontal resolution of $1° \times 1°$ is derived from the Met Office Hadley Centre SST dataset (HadISST1; Rayner 2003) to display the evolution of IOD events. Atmospheric data including surface wind and sea level pressure (SLP) are obtained from the National Centers for Environmental Prediction-National Center for Atmospheric Research (NCEP/NCAR) Reanalysis with a $2.5° \times 2.5°$ resolution (Kalnay et al. 1996). The datasets above cover the period from 1948 to 2022.

Ocean potential temperature, oceanic circulation data, net surface heat flux, and sea surface height (SSH) are all derived from the NCEP Global Ocean Data Assimilation System (GODAS) product (Behringer et al. 1998). The SSH anomaly (SSHA) is used as a proxy to represent the variation of the thermocline depth. The outgoing longwave radiation (OLR) is derived from National Oceanic and Atmospheric Administration (NOAA; Liebmann and Smith 1996). The OLR is regarded as a proxy for deep convection, clouds, and precipitation in the tropical region. The positive (negative) OLR anomaly (OLRA) represents negative (positive) rainfall and suppressed (enhanced) convection. The monthly outputs above cover the period from 1980 to 2022. The four components of surface heat flux (latent heat flux, sensible heat flux, longwave radiation, and shortwave radiation) available from 1984 to 2009 are supported by Objectively Analyzed air-sea

Fluxes for the global oceans (OAFlux; Yu and Weller 2007). After removing the monthly mean climatology, all variable anomalies presented in this study are detrended to eliminate the long-term trends.

To demonstrate the robustness of the results, we also checked the SST data from the NOAA SST ERSST monthly v5 (Huang et al. 2017) and obtained similar results. We also perform the mixed layer heat budget analysis using the SODA 3.3.1 (Carton et al. 2018) and the Ocean Reanalysis System 5 (ORAS5) data (Zuo et al. 2019). The four components of surface heat flux from the ECMWF Reanalysis v5 (ERA5; Hersbach et al. 2020) dataset is utilized to investigate processes being responsible for changes in net heat flux.

2.2 Methods

2.2.1 Classification of IOD events

The Dipole Mode Index (DMI) is defined as the difference in the averaged SSTAs between the WIO (10° S–10° N, 50° E–70° E) and the southeastern TIO (10° S–0°, 90° E–110° E), following Saji et al. (1999). An IOD event is defined when the three-month moving average of DMI exceeds one standard deviation during the peak season. We mainly focus on the pIOD events in this study. Some IOD events peak in boreal summer (June–July–August, JJA), while some others mature in boreal autumn (September–October–November, SON). Thus, the IOD events are divided into two groups based on the peak season in this study, i.e., the summer IOD and the autumn IOD. From 1948 to 2022, eight summer IOD events and eight autumn IOD events are identified, consistent with the findings of previous studies (e.g. Sun et al. 2014; Zhang et al. 2019).

2.2.2 Mixed layer heat budget analysis

To understand the ocean–atmosphere coupling processes responsible for the evolution of the western and the eastern poles, we conduct the mixed layer heat budget analysis (Vijith et al. 2020) for the summer IOD and the autumn IOD. The mixed layer heat budget equation is derived as follows,

$$\frac{\partial T}{\partial t} = Q - \left(u\frac{\partial T}{\partial x} + v\frac{\partial T}{\partial y}\right) - \left(\frac{T - T_{-h}}{h}\right)w_e + R \tag{1}$$

Variables T, u, and v represent potential temperature, zonal and meridional ocean current velocity averaged within the mixed layer, respectively. Variables w and h represent vertical velocity and the mixed layer depth (MLD). Suffix $-h$ denotes the quantity at the base of the mixed layer. The terms in Eq. 1 from left to right, are the mixed layer temperature (MLT) tendency, net heat flux, horizontal advection, entrainment, and residual term.

The w_e in the entrainment term can be decomposed into the ML tendency, vertical advection and lateral induction, which is given by,

$$w_e = \frac{\partial h}{\partial t} + w_{-h} + u_{-h}\frac{\partial h}{\partial x} + v_{-h}\frac{\partial h}{\partial y} \tag{2}$$

Q represents the net air-sea heat flux retained within the mixed layer. Further, Q can be decomposed into the Q_0 and Q_{pen}, where Q_0 is the net surface heat flux and Q_{pen} is the shortwave radiation that penetrates the base of the mixed layer. ρ_0 is the density of water (1026 kg m^{-3}), C_p is the specific heat capacity of water (3986 J kg^{-1} K^{-1}).

$$Q = \frac{Q_0 - Q_{pen}}{\rho_0 C_p h} \tag{3}$$

Q_0 is defined as the sum of the latent heat flux (LH), sensible heat flux (SH), shortwave radiation (SW) and longwave radiation (LW) at surface.

$$Q_0 = LH + SH + SW + LW \tag{4}$$

Q_{pen} is estimated as (Paulson and Simpson 1977; Santoso et al. 2010),

$$Q_{pen} = SW\left[Re^{(-h/\gamma_1)} + (1-R)e^{(-h/\gamma_2)}\right], \tag{5}$$

where $R = 0.67$, $\gamma_1 = 1$ and $\gamma_2 = 17$ (Dong et al. 2007).

After performing the Reynolds decomposition analysis for Eq. 1, we obtain the Mixed layer heat budget equation as follows,

$$\frac{\partial T'}{\partial t} = Q' - \left(u'\frac{\partial \overline{T}}{\partial x} + \overline{u}\frac{\partial T'}{\partial x} + u'\frac{\partial T'}{\partial x} + v'\frac{\partial \overline{T}}{\partial y} + \overline{v}\frac{\partial T'}{\partial y} + v'\frac{\partial T'}{\partial y}\right) - \left(\frac{T' - T'_{-h}}{h}\overline{w_e} + \frac{\overline{T} - \overline{T_{-h}}}{h}w'_e + \frac{T' - T'_{-h}}{h}w'_e\right) + R, \tag{6}$$

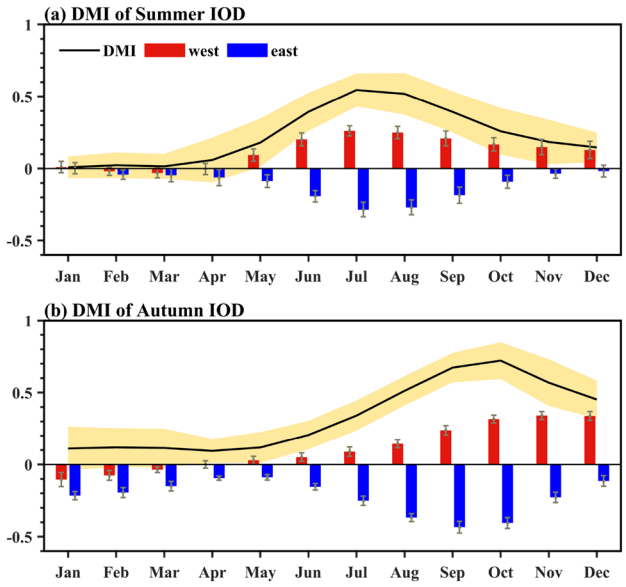

Fig. 1 Temporal evolution of the DMI (solid line, units: °C), SSTAs averaged over the western pole (red bar, units: °C) and the eastern pole (blue bar, units: °C) of the summer IOD in (**a**) and the autumn IOD in (**b**). Solid black line represents the mean values of HadISST and ERSST whereas shading represents a 0.5 standard deviation of the DMI. The error bars represent 1 standard error

where overbars and primes present the monthly climatology and anomaly, respectively.

3 Results

3.1 Characteristics of the summer IOD and the autumn IOD

Two types of IOD events with distinctive phase-locking features are presented in this study. The summer IOD develops rapidly in early boreal spring and reaches its mature phase in July (Fig. 1a), while the autumn IOD develops from late spring to autumn and peaks around October (Fig. 1b). It can be noticed that the western and eastern poles of the summer IOD develop simultaneously, while the eastern pole of the autumn IOD precedes the western pole for nearly one season (Fig. 1). The growth rate of the western pole of the autumn IOD seems to be suppressed in summer, significant positive SSTAs in the western pole are therefore absent before August (Figs. 1b and 2e, 7 of 8 autumn IOD events display this feature). Although the eastern pole of both the summer IOD and the autumn IOD begins to develop in JJA, that of the autumn IOD is characterized by a longer lifetime owing to stronger easterly wind anomalies in SON (Fig. 2e, f). With the intensification of the easterly wind anomalies, warm SSTAs are formed in the WIO of the autumn IOD (Fig. 2f). That is to say, these strong easterly winds may be crucial to the formation of not only the cold SSTAs in the eastern pole but also the warm SSTAs in the western pole, leading to the occurrence of autumn IOD. The associated ocean–atmosphere coupling processes will be discussed in Sect. 3.2.

The spatial evolution of the summer IOD and autumn IOD also displays large differences (Fig. 2). The broad-scaled warm SSTAs of the western pole are observed to be close to the central Indian Ocean during JJA in the summer IOD years (Fig. 2b). The warm sea surface during the summer monsoon season is favorable for the enhancement of convection and the induced local air-sea interactions in the WIO. However, warm SSTAs of the autumn IOD are absent until SON and locate more to the west intruding into Somalia's coastal region, indicating distinctive underlying mechanisms for the development of the two types of IOD events.

The discussion above points out that the temporal-spatial characteristics of the summer IOD and autumn IOD are remarkably different. The summer IOD is featured by warm SSTAs in the WIO during JJA, while the autumn IOD is characterized by strong easterly wind anomalies during SON, implying distinctive ocean-atmospheric couplings may be responsible for their development. The autumn IOD is similar to the canonical IOD described in previous studies (Saji et al. 1999; Webster et al. 1999), the mature phase of which lags behind the summer IOD resembling the unseasonable IOD proposed by Du et al. (2013) by nearly 3 months. We will further investigate the dynamic and thermodynamic processes responsible for the two types of IOD events, in terms of both the western and eastern poles.

3.2 Mechanisms

3.2.1 Warming in the western pole

The warm western pole of the summer IOD mostly develops during JJA, while that of the autumn IOD primarily occurs in SON (Fig. 2), suggesting that the underlying mechanisms might differ between the two types of IOD events.

For the summer IOD, the warming tendency of WIO SSTAs during March-August is mainly contributed by changes in both the oceanic dynamics and the net surface heat flux (Fig. 3a). The oceanic dynamics especially the entrainment over the WIO is presented to be important at an early stage of the developing phase (Fig. 2a). These features may act as precursors to the WIO warming for the summer IOD. However, after June, the relatively weak oceanic processes in the WIO are insufficient to maintain the warm mixed layer temperature (MLT) tendency (Fig. 3a), which may be related to the absence of strong equatorial easterly wind anomalies (Fig. 2b, c).

During boreal summer, the surface heat flux takes the role of oceanic advection in contributing to the warm WIO

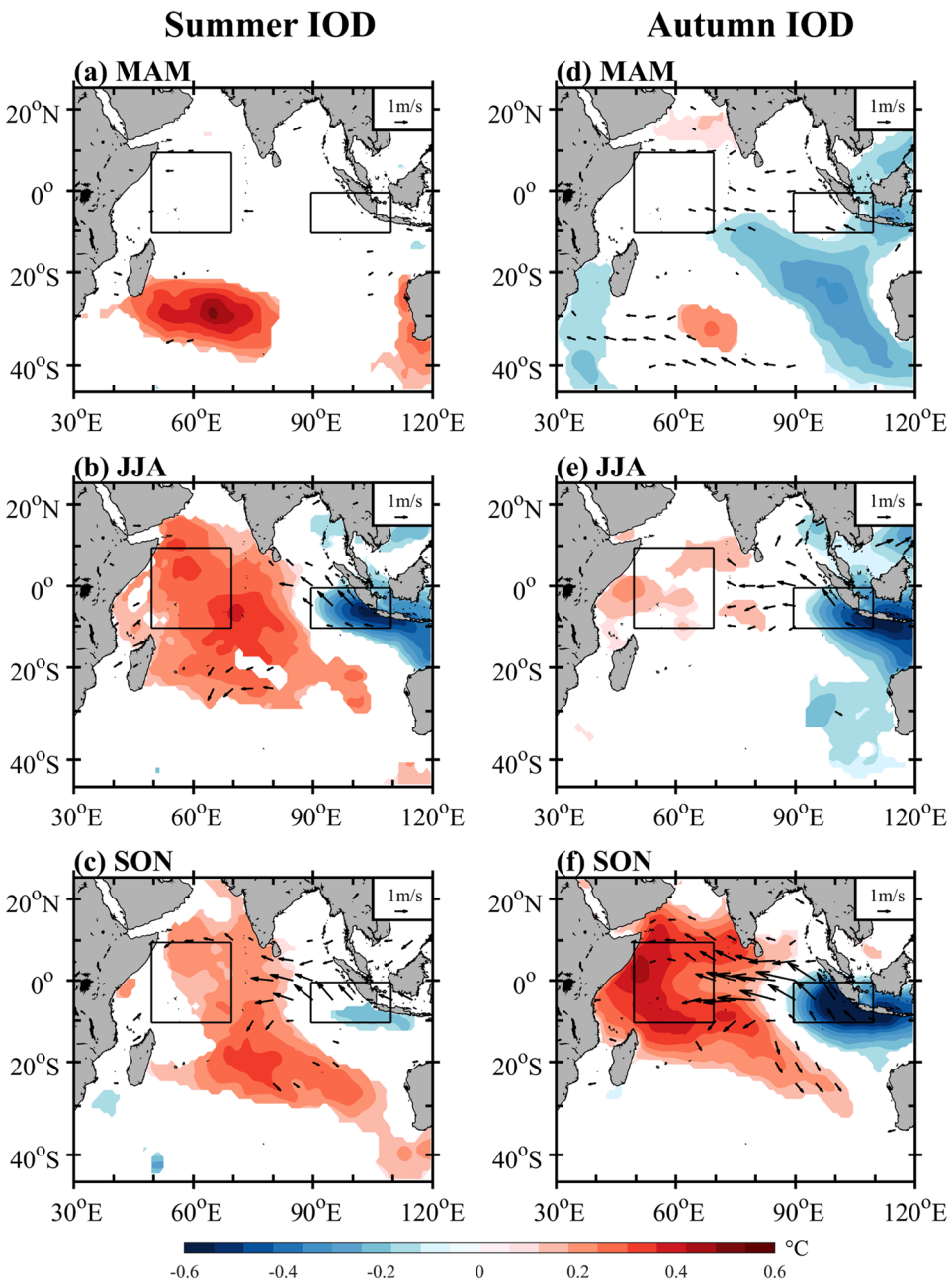

Fig. 2 Composite of SSTAs (shading, units: ℃) and surface wind anomalies (vectors, units: m s^{-1}) for the summer IOD (**a**–**c**) and the autumn IOD (**d**–**f**), from the developing spring to the succeeding autumn. Datasets for SST: HadISST and ERSST. Black boxes on the left and right respectively indicate the location of the western pole (10° S–10° N, 50° E–70° E) and the eastern pole (10° S–0°, 90° E–110° E). Only values at the 90% confidence level according to a two-tailed Student's *t*-test are shown

SSTAs (as shown in Figs. 3a and 4a). The positive latent heat flux and longwave radiation downward into the upper ocean are responsible for the large amplitude of net surface heat flux, which in turn is related to the weakened wind speed and enhanced convection in the WIO (Figs. 5a–c and 6b). In the western pole, the decrease in wind speed (Fig. 5a, b) leads to a reduction in sea surface latent heat loss, facilitating the formation of warm SSTAs. Additionally, the strong convection (denoted by the negative OLRA; Fig. 6b) over the WIO also contributes to the positive effect of longwave radiation. Although the SST-cloud-radiation feedback causes a reduction in shortwave radiation into the sea surface (as shown in Fig. 4a), the warm SSTAs in the WIO lead to an increase in water vapor, further promoting atmospheric convection and longwave radiation reflected into the ocean. Thus, the dominant factors in the warm growth rate of the western pole of summer pIOD during JJA are the vigorous latent heat flux and longwave radiation into the upper ocean (as depicted in Fig. 4a).

In contrast to the summer IOD, the western pole of the autumn IOD experiences a delay in warming, with warm SSTAs not being evident until September (Fig. 3c). During JJA, the relatively weak atmospheric and oceanic processes are insufficient to warm the cooler sea surface in

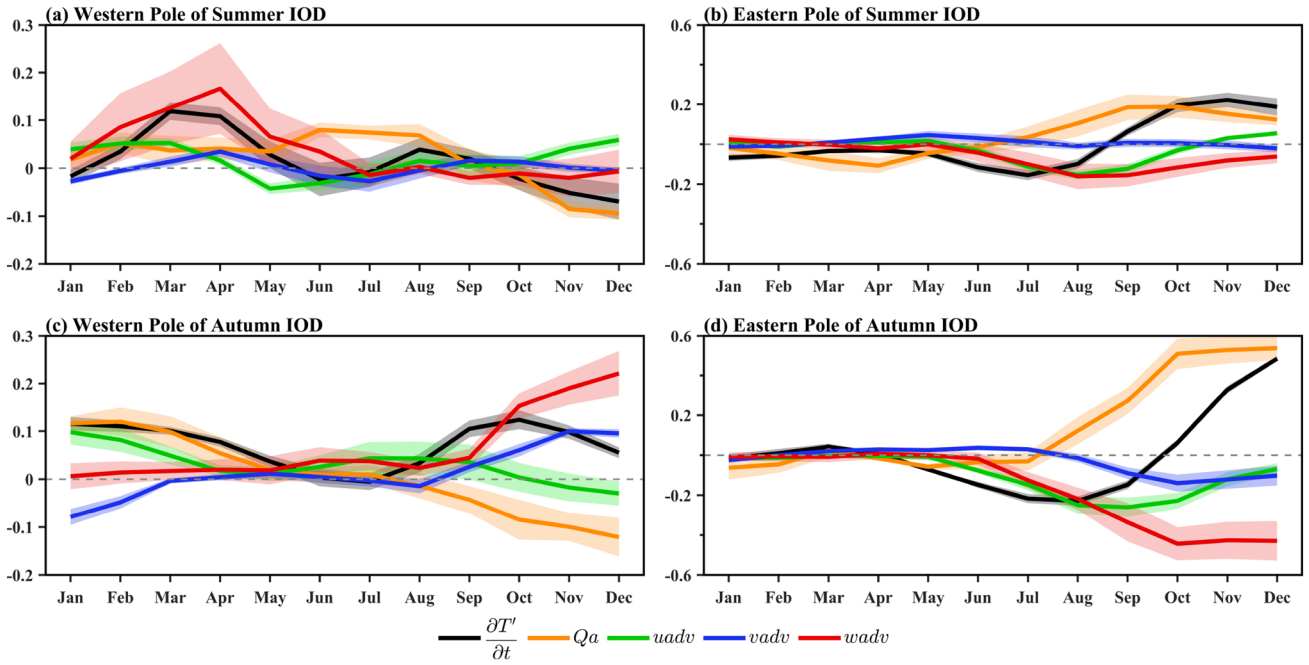

Fig. 3 Composite monthly evolution of the MLT tendency ($\partial T'/\partial t$, black bold solid line, units: °C month^{-1}), the net surface heat flux term (Q_a, orange solid line, units: °C month^{-1}), the total zonal advection (green solid line, units: °C month^{-1}), the total meridional advection (blue solid line, units: °C month^{-1}), the entrainment term (red solid line, units: °C month^{-1}) for (**a**) the western pole of summer IOD, (**b**) the eastern pole of summer IOD, (**c**) the western pole of autumn IOD, and (**d**) the eastern pole of autumn IOD. The MLT tendency and oceanic processes are averaged across the GODAS, SODA, and ORAS5 datasets. The net surface heat flux is averaged across the OAFlux and ERA5 datasets. Shading represents 1 standard deviation

MAM (Fig. 2d), resulting in the absence of upper-ocean warming in the WIO during summertime. However, the positive MLT tendency of the western pole is rapidly established during SON, reaching its peak in October due to strong oceanic processes (Fig. 3c). This warming tendency is counteracted by the net surface heat flux, particularly shortwave radiation, which impedes the warming tendency. Despite this, the strong upper-ocean meridional advection and entrainment are sufficient to offset the negative net surface heat flux, indicating the dominance of oceanic processes for the western pole of the autumn IOD. These findings suggest that the ocean–atmosphere coupling processes responsible for the evolution of the western pole of the autumn IOD differ from those of the summer IOD, with oceanic processes playing a more dominant role.

Compared to the summer IOD, easterly wind anomalies are stronger during the autumn IOD in JJA, and they rapidly strengthen in SON (Fig. 2), leading to stronger responses in the upper ocean of the WIO. Westward propagating off-equatorial downwelling Rossby waves are observed during autumn IOD years (Fig. 7b), and the Ekman pumping feedback ($-w'\partial\overline{T}/\partial z$) associated with anomalous descending motions plays a dominant role compared to other terms (Fig. 4c). The Rossby waves originate in the southeastern TIO (~ 80° E), propagate westward along 10° S–8° S (Fig. 7b), and reach the WIO after about three months with a phase speed of approximately 0.2 m s^{-1} (consistent with previous studies Xie et al. 2002; Huang et al. 2020; Zhang and Du 2022). Correspondingly, significant warm SSTAs appear in the western pole and reach the maximum in SON (Fig. 2f). It can be noticed that the warming spreads to the east coast of North Africa as easterly wind anomalies intrude further west (Fig. 2f). It is reasonable to assume that the formation of the western pole of the autumn IOD is closely related to the intensive easterly winds. Previous studies also proposed that the strong easterly wind anomalies along the equator and anticyclonic wind stress curl over the off-equatorial region can not only drive warm water accumulated westward (Guo et al. 2015; Jiang et al. 2022) but also excite the westward downwelling Rossby waves (Cai et al. 2021), facilitating the warm SSTAs in the western pole (Murtugudde and Busalacchi 1999; Xie et al. 2002; Du et al. 2020). Hence, these wind-induced downwelling Rossby waves are essential to the warming SSTAs in the western pole of the autumn IOD.

Overall, the dynamic processes accounting for the western pole of the two types of pIOD events are significantly different. During summer pIOD years, positive SSTAs in the WIO primarily result from local ocean–atmosphere

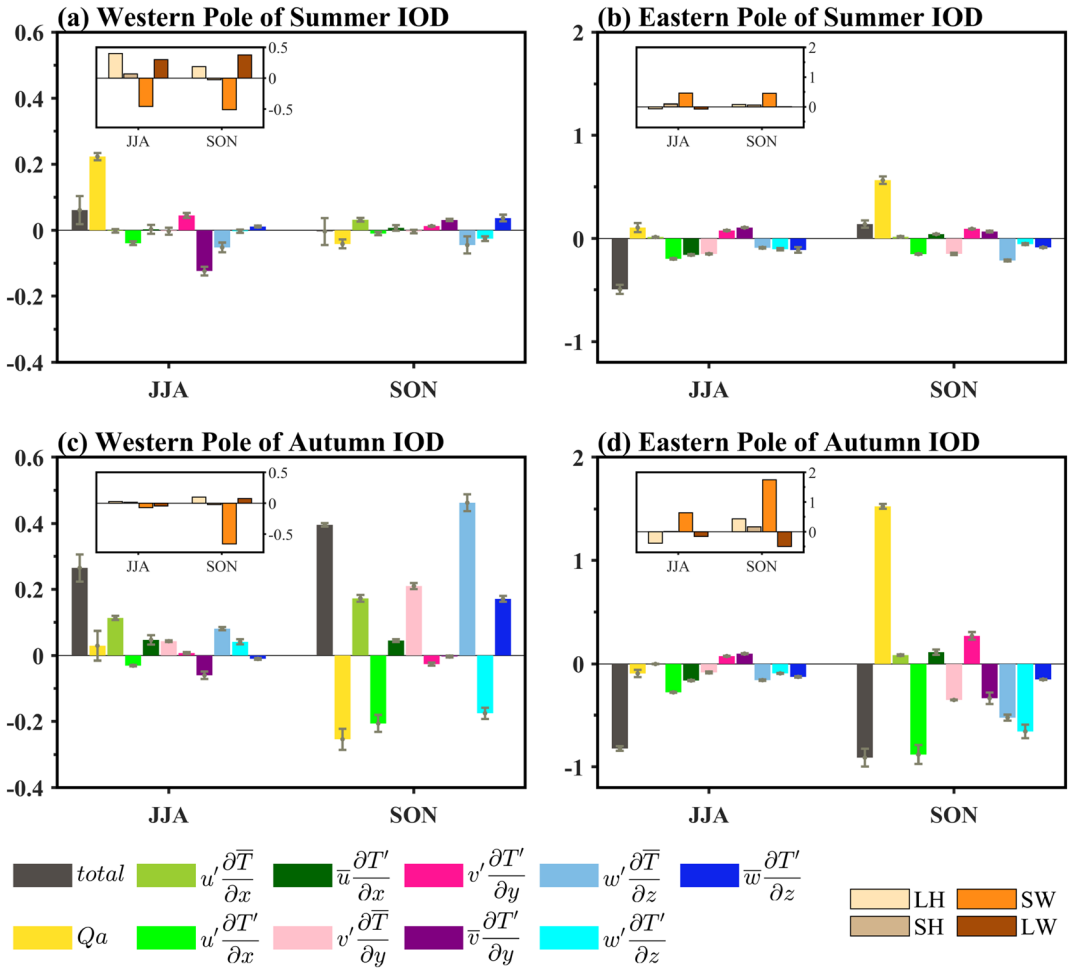

Fig. 4 Composite of the heat budget terms in JJA and SON (units: °C month^{-1}) over (**a**) the western pole of summer IOD, (**b**) the eastern pole of summer IOD, (**c**) the western pole of autumn IOD, and (**d**) the eastern pole of autumn IOD. The subplots represent the four components of net surface heat flux, namely the latent heat flux (LH), sensible heat flux (SH), shortwave radiation (SW), and longwave radiation (LW). The MLT tendency and oceanic processes are averaged across the GODAS, SODA, and ORAS5 datasets. The net surface heat flux is averaged across the OAFlux and ERA5 datasets. The error bars represent 1 standard error

feedback, particularly the positive downward latent heat flux and longwave radiation induced by enhanced convection. However, oceanic processes associated with downwelling Rossby waves dominate the formation of the western pole of the autumn pIOD, which is closely related to the strong easterly wind anomalies.

3.2.2 Cooling in the eastern pole

Negative SSTAs emerge along the Java/Sumatra coastal region during boreal summer, coinciding with the establishment of the Indian summer monsoon in both types of pIOD years. The formation of the cold eastern pole is closely related to the prevailing easterly wind anomalies over the EIO. During this monsoonal season, intensified easterly winds further shoal the thermocline and enhance coastal upwelling off Java/Sumatra, triggering the positive Bjerknes feedback (Bjerknes 1969), resulting in negative zonal advection and vertical advection in the eastern TIO, which are mostly in phase with the MLT cooling tendency (Fig. 3b, d). This indicates the importance of oceanic dynamics in the development of the eastern pole of IOD events. Easterly wind anomalies can also cool the eastern pole via wind-evaporation-SST feedback (WES; Xie and Philander 1994). The acceleration of the wind speed (Fig. 5b, e) and greater latent heat loss (Fig. 4b, d) from the EIO sea surface can be noticed in JJA. The amplitude of the anomalous latent heat flux is observed to be larger in autumn IOD, corresponding to stronger easterly anomalies in the EIO (Fig. 2c, f). Although changes in the latent heat flux are conducive to cooling the eastern pole, shortwave radiation dominates the net surface heat flux and acts as a damping term in both types of IOD (as shown in Hong et al. 2008c). This is because the negative SSTAs suppress atmospheric

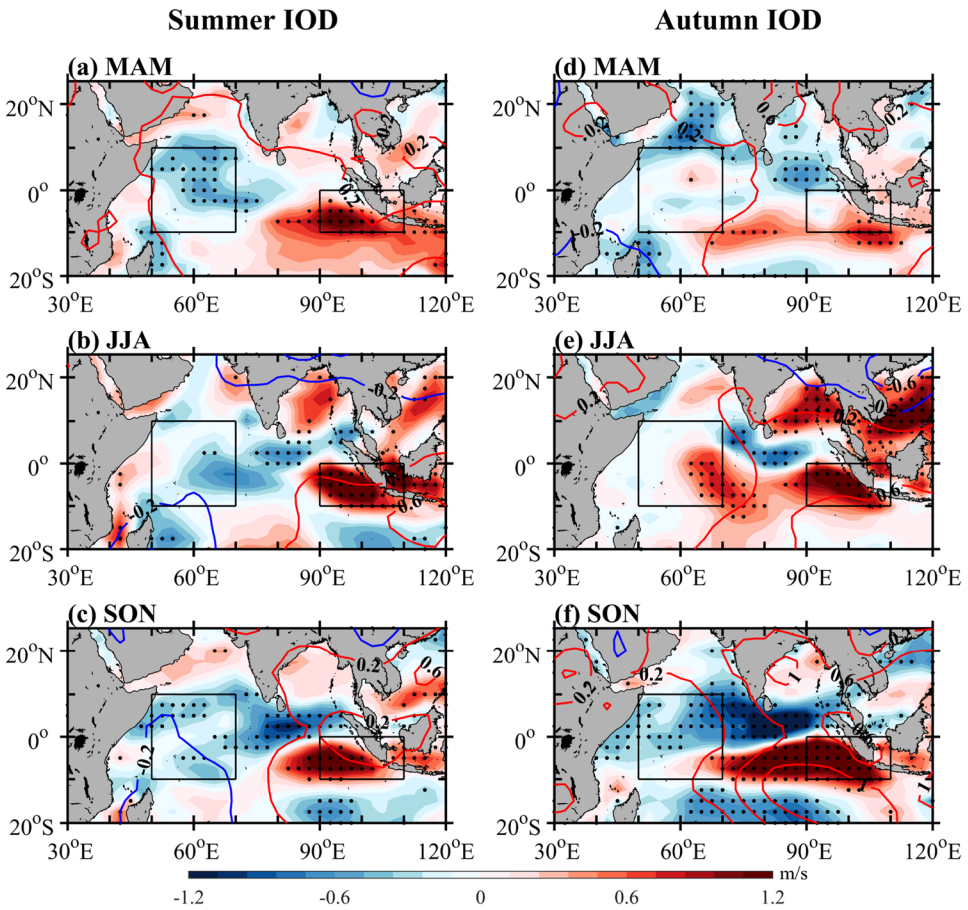

Fig. 5 Composite of wind speed anomalies (shading, units: m s^{-1}) and SLPA (contour, units: hPa) for the summer IOD (**a**–**c**) and the autumn IOD (**d**–**f**), from the developing spring to the succeeding autumn. Wind speed anomalies at the 90% confidence level according to a two-tailed Student's *t*-test are dotted

convection over the EIO in JJA (Fig. 6), which reduces the cloud amount (positive OLRA) and leads to positive downward shortwave radiation into the upper ocean (Fig. 4b, d, as shown in Francis et al. 2007). In the succedent autumn, with the intensification of negative SSTAs and weakened convection, the damping effect of net heat flux rapidly increases, especially in the autumn IOD years with a colder underlying sea surface (Fig. 4d). However, the cold SSTAs in the eastern Indian Ocean still possesses a longer lifetime in the autumn IOD years compared to the summer IOD years.

The differences in the evolution of the eastern pole may be related to changes in easterly winds (Fig. 2c, f) and associated oceanic dynamics. During SON, the intensity of horizontal advection and entrainment weakens in summer IOD years (as seen in Fig. 3b). These oceanic processes are insufficient to offset the effect of the positive net surface heat flux, resulting in a gradual decline in the cooling tendency in the eastern pole during the summer IOD. However, oceanic advection continues to develop in SON and is strong enough to overwhelm the damping effect of the positive net surface heat flux (Fig. 3d). The cooling tendency associated with the ocean dynamical processes in the autumn IOD is approximately five times stronger than that in the summer IOD during this season (Fig. 4b, d). The autumn IOD is therefore characterized by a longer lifetime. Previous studies have also pointed out that nonlinear oceanic advection is critical to the formation of IOD (Halkides and Lee 2009; Ng et al. 2015; Cai et al. 2021). As shown in Fig. 4d, nonlinear advection, which is related to the Bjerknes feedback, dominates over other processes during SON. The stronger ocean dynamic processes are closely related to the remarkable intensive easterly winds persisting in SON (Fig. 2f), which dominate the formation and long persistence of the dipole SSTA pattern of the autumn IOD. The source of the easterly winds observed in the autumn IOD could be attributed to the remote forcing of ENSO, which will be discussed in the next section.

3.3 Differences in the ENSO-IOD relationship

The composite patterns of the two types of IOD events indicate that autumn IOD events are intimately related to

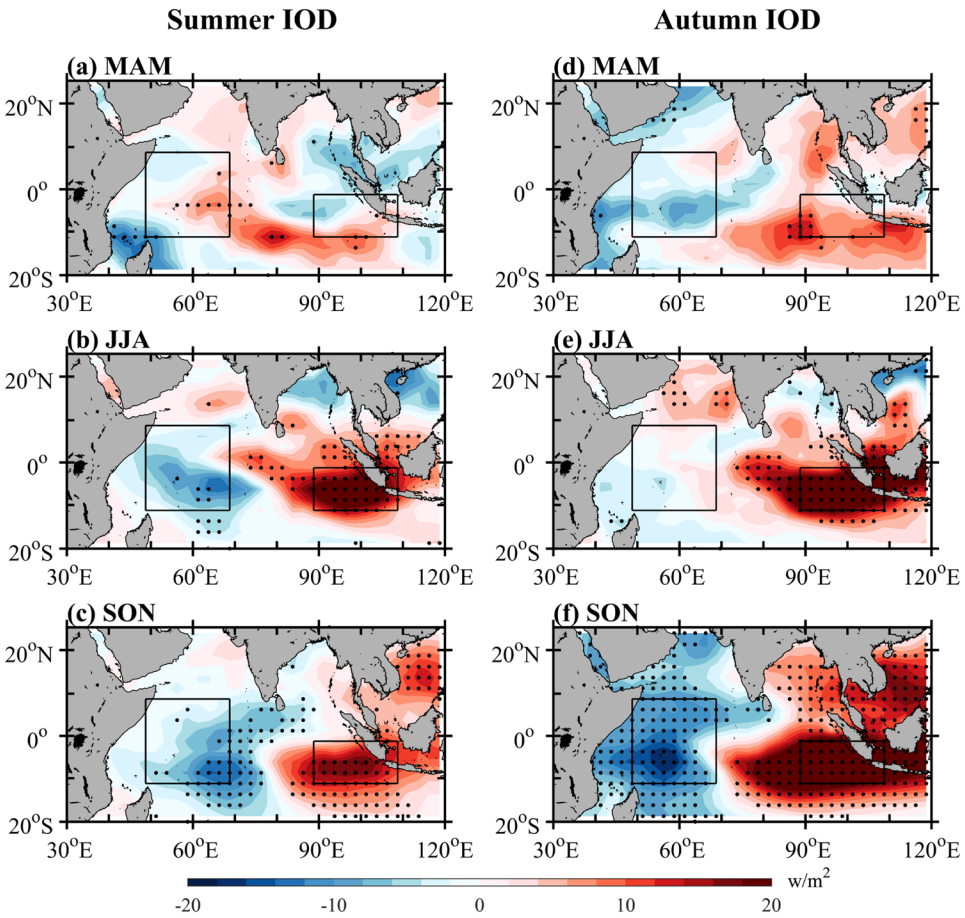

Fig. 6 Composite of OLR anomalies (shading, units: W m^{-2}) for the summer IOD (**a**–**c**) and the autumn IOD (**d**–**f**), from the developing spring to the succeeding autumn. Values at the 90% confidence level according to a two-tailed Student's *t*-test are in black dots

ENSO (Fig. 10). We perform a lead regression to remove the succeeding Niño 3.4 index (mean value of the Niño3.4 index during December(0)–January(1)). The occurrence of autumn IOD events during 1948–2022 is reduced from 8 to 3 after removing the succeeding Niño 3.4 index (Table 1), demonstrating that the autumn IOD is strongly modulated by ENSO variability. The monthly evolution of summer IOD and autumn IOD after removing the effect of ENSO has been shown in Fig. 8. Compared with Fig. 1, it can be observed that the amplitude of the DMI and SSTA averaged over both the western and eastern poles of the autumn IOD largely decreases when the impact of ENSO is removed (Figs. 1b, 8b, and 9f), indicating that ENSO contributes significantly not only to the eastern pole but also to the western pole of the autumn IOD. While those amplitude in the summer IOD have hardly changed. The result indicates that ENSO has little effect on the summer IOD but strongly affects the autumn IOD.

Easterly wind anomalies are crucial for the development of the eastern pole of IOD, as mentioned before. However, the spatial distribution, intensity, and persistence of these anomalies differ between the summer IOD and autumn IOD (Fig. 2). During the development of the summer IOD, anomalous easterly winds are concentrated in a narrow belt and are more restricted to the EIO, while during the autumn IOD, they feature a broader meridional pattern and extend more to the west (Fig. 2). Further studies indicate that the strong easterly wind anomalies during the autumn IOD are related to the El Niño accompanied intensification of the Australian high (Figs. 5f and 10d–f). During the developing phase of the ENSO, noticeable positive SLPA in the Australian region can be observed. The enhanced Australian high is favorable for the strengthened easterly wind anomalies during the autumn IOD, which in turn are conducive to the development of oceanic processes via positive Bjerknes feedback, corresponding to the strong zonal advection and entrainment in SON (Fig. 4d). That's to say, the persistence of the autumn IOD is mainly attributed to the El Niño accompanied Australian high anomaly. However, these atmospheric responses to ENSO are absent in summer IOD years (Fig. 10a–c), demonstrating that ENSO has little effect on the summer IOD. During the summer IOD, owing to the lack of strong positive SLPA over the Australian continent in SON (Fig. 5c), the easterly wind anomalies along the Java/Sumatra coastal region are relatively weak (Fig. 2c). Therefore, the summer IOD events gradually decline in SON. This result is consistent with our finding that local

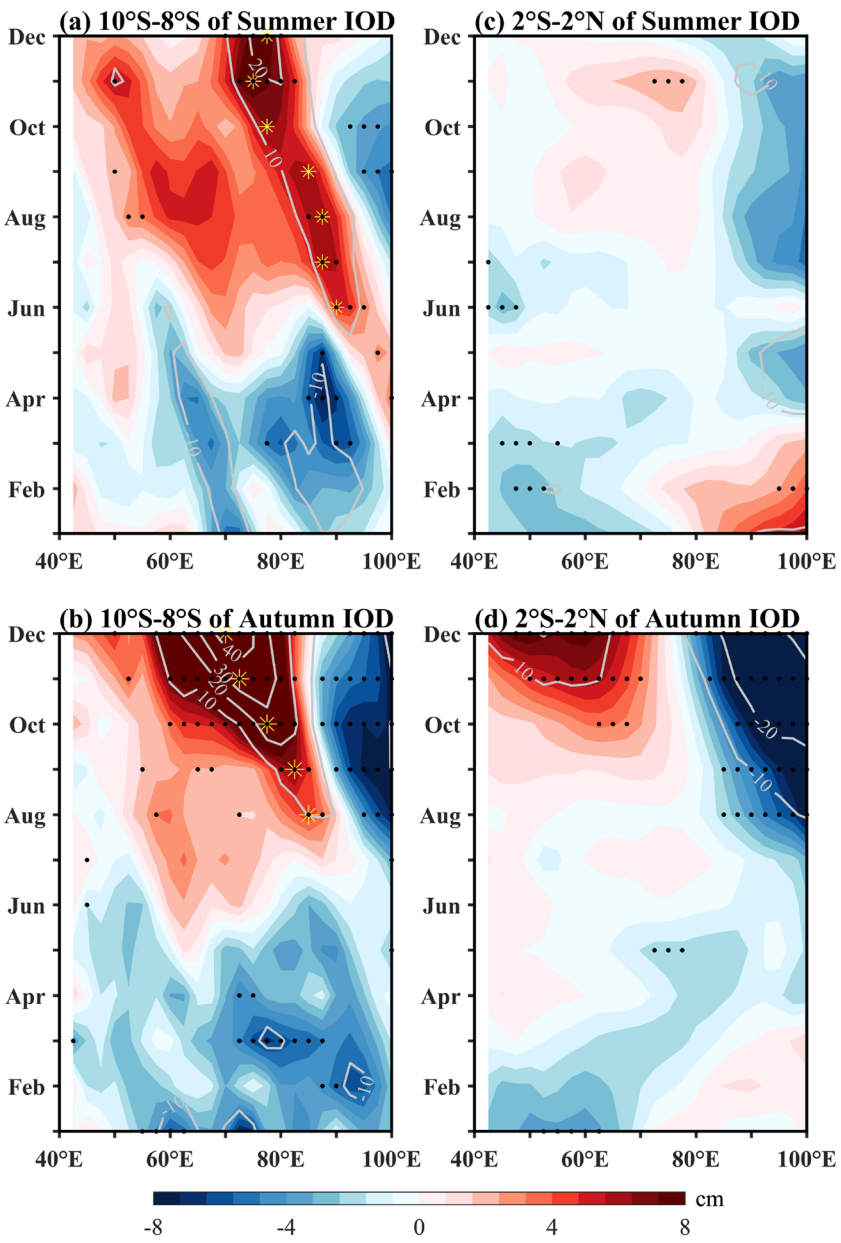

Fig. 7 Time-longitude diagrams of anomalous SSH (shading, units: cm) and thermocline depth (contour, units: m) averaged in the off-equatorial region (10° S–8° S) and the equatorial Indian Ocean (2° S–2° N) for the summer IOD (**a**, **c**) and the autumn IOD (**b**, **d**). Values at the 90% confidence level are in black dots. The yellow asterisk represents the maximum value of the positive SSHA

air-sea interactions in the Indian Ocean play a crucial role in the evolution of the summer IOD.

The differences in the ENSO-IOD relationship have a significant impact on the evolution of the eastern and western poles of the two types of IOD events. The eastern pole of the autumn IOD has a longer lifetime than that of the summer IOD. The growth rate of the autumn IOD is much larger due to strong easterly wind anomalies along the equatorial Indian Ocean, intimately related to ENSO. These anomalies persist until boreal winter and have a larger amplitude, making autumn IOD events much stronger than summer ones. The zonal wind anomalies also contribute to the formation of the western pole via the oceanic downwelling Rossby waves. However, atmospheric processes dominate the evolution of the short-lived summer IOD. Thus, ENSO is the primary external forcing that promotes and prolongs the growth of IOD events. Large-scale atmospheric responses to ENSO variability effectively fuel the development of the autumn IOD, while they are absent in summer IOD years (Fig. 10).

Table 1 The summer IOD events and the autumn IOD events during 1980–2020. The event in bold denotes the one still robust after removing ENSO

Summer IOD	**1961, 1972, 1976,** 1991, **1994, 2012,** 2015, **2017**
Autumn IOD	1951, 1963, **1967,** 1982, **1997,** 2006, **2018,** 2019

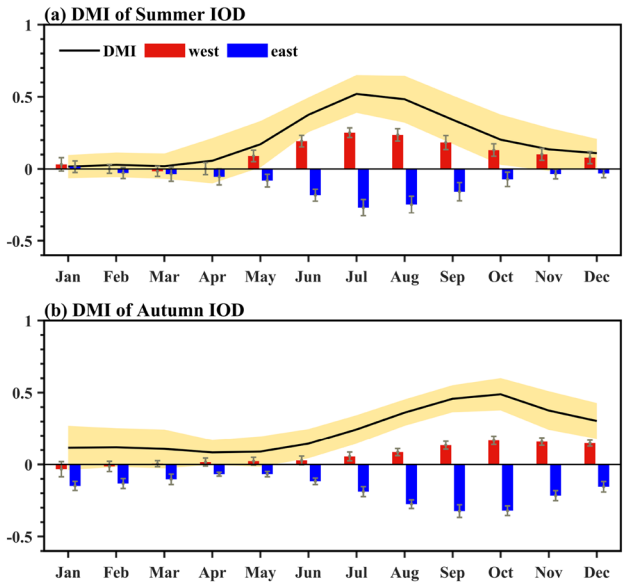

Fig. 8 Same as Fig. 1, but for using SSTAs with the influence of ENSO excluded. ENSO variability is represented by Niño 3.4 index, which is defined as the SSTAs averaged over the tropical Pacific region (5° S–5° N, 170° W–120° W). The solid black line represents mean values of HadISST and ERSST whereas shading represents a 0.5 standard deviation of the DMI. The error bars represent 1 standard error

4 Summary and discussion

In this study, we have shown that the summer IOD and the autumn IOD, respectively mature in boreal summer and autumn, exhibit distinctive temporal-spatial characteristics resulting from different climate dynamic processes. The summer IOD benefits from broad-scaled warm SSTAs in the WIO, which enhance local air-sea interactions and easterly wind anomalies in the EIO through the east–west temperature gradient. The warm sea surface promotes local atmospheric convection and reduces surface wind speed. Then it induces strong positive longwave radiation reflected back to the upper ocean and less latent heat loss from the sea surface, which in turn lead to a rapid growth of warming in the western pole of the summer IOD. Additionally, the eastern pole begins to develop through positive Bjerknes feedback when the Indian summer monsoon prevails in June and then decays as the monsoon system retreats. Thus, the summer IOD is primarily influenced by the air-sea interactions intrinsic to the Indian Ocean, particularly in the WIO.

Conversely, for the autumn IOD, strong easterly wind anomalies extending from the eastern TIO to the central TIO play a crucial role in the development of both the western and eastern poles. Once these wind anomalies prevail off Sumatra/Java, the positive Bjerknes feedback and WES feedback contribute to the establishment of cold SSTAs in the EIO. The intensified equatorial easterly winds can also induce off-equatorial anticyclonic wind stress curl that excites downwelling Rossby waves, further warming SSTAs in the WIO via oceanic processes. Thus, the evolution of the eastern pole precedes that of the western pole, similar to the formation of the canonical IOD shown in previous studies (Wang et al. 2019). Additionally, the eastern pole associated with strong easterly wind anomalies dominates the formation of the autumn IOD (Luo et al. 2010).

The easterly wind anomalies during autumn IOD years are fueled remotely by El Niño events in the tropical Pacific. As a response to El Niño, positive SLPA with anticyclonic atmospheric circulation is observed over the Maritime Continent region and the southeastern TIO (as also shown in Yu and Rienecker 1999), and these anomalous easterly winds off Sumatra/Java can persist into SON. The El Niño accompanied Australian high anomaly is favorable for the strengthened easterly wind anomalies, which in turn are conducive to the development of the eastern and western pole of autumn IOD via oceanic processes. However, these atmospheric responses to ENSO are absent in summer IOD years. During the summer IOD, owing to the lack of strong positive SLPA over the Australian continent in SON, the easterly winds generated by air-sea interactions intrinsic to the Indian Ocean are weaker and short-lived. Therefore, the summer IOD events gradually decline in SON. The climate dynamic processes responsible for the two distinctive types of IOD events have been illustrated in Fig. 11. Local air-sea interactions intrinsic to the Indian Ocean are vital for the formation of the IOD with an earlier peak season, while ENSO can be regarded as the predominant external forcing that promotes and prolongs the growth of IOD events. Yang et al. (2015) reached a similar conclusion that the internal IOD starts to develop in June, while the ENSO-related IOD lags about two months. Thus, the climate dynamics underlying the evolution of the eastern and western poles of the summer IOD and the autumn IOD are different. Our results can help to deepen the understanding of IOD events through comprehensive analyses of IOD diversity.

We have also preliminarily attempted to apply the CMIP6 historical simulation data to study the spatial–temporal characteristics of the two types of IOD events. The CMIP6 simulations results show that some IOD events tend to peak in JJA, and the spatial–temporal characteristics of the summer IOD are consistent with the conclusion in observations. While the warming of the WIO during autumn IOD tends to present in summer, which is slightly different from the feeble response of the WIO in observation. It might be due to an overestimation of the responses of Indian Ocean air–sea coupling strength to ENSO in climate model simulations (Zhang et al. 2021; Zhong et al. 2023). Thus, it is necessary to make further studies on the performance of CMIP models in simulating different types of IOD events.

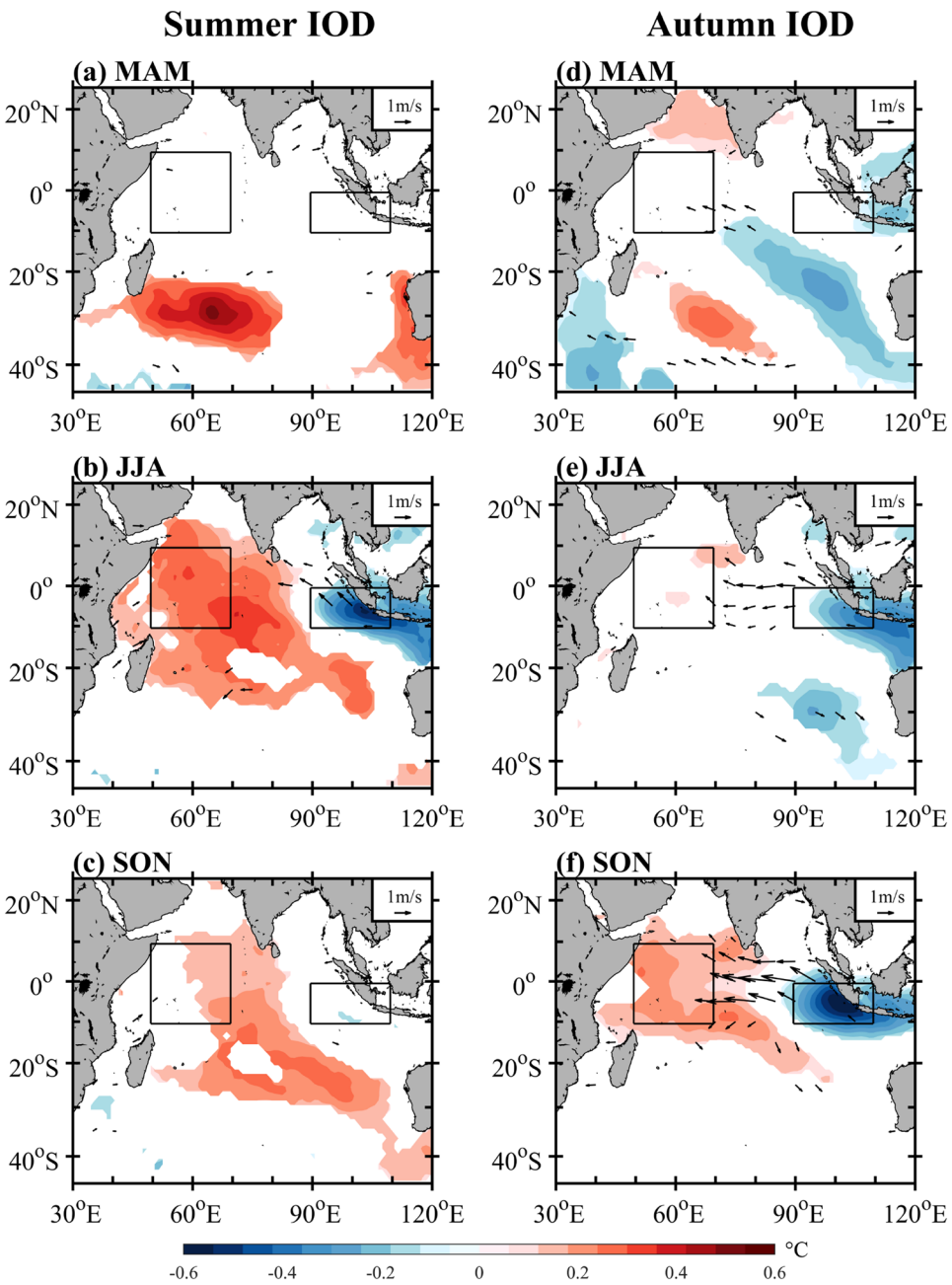

Fig. 9 Composite of SSTAs (shading, units: ℃) and surface wind anomalies (vectors, units: m s^{-1}) that exclude the influence of ENSO for the summer IOD (**a**–**c**) and the autumn IOD (**d**–**f**), from the developing spring to the succeeding autumn. Datasets for SST: HadISST and ERSST. Only values at the 90% confidence level according to a two-tailed Student's *t*-test are shown

Previous studies have shown that the mid-high latitude climate signals in the southern Indian Ocean can trigger the onset of the IOD independently of ENSO (Fischer et al. 2005). The Southern Annular Mode (SAM) is an influential climate signal in the Southern Hemisphere (Rogers and Loon 1982; Thompson and Wallace 2000). Some studies suggest that SAM can promote IOD-conducive wind anomalies via extratropical SLP fluctuations (Lau and Nath 2004), while others found that SAM cannot significantly impact the IOD (Cai et al. 2011a). It seems that the interaction between the high-latitude SAM and tropical IOD is still under debate. Moreover, a mode resembling the SIOD in the subtropical southern IO can be observed in the initial phase of the autumn IOD (Fig. 2d). The SIOD associated with the Mascarene high is supposed to be an important trigger for the IOD occurring several months later (Terray et al. 2007; Feng et al. 2014; Zhang et al. 2018). Zhang et al. (2020) further proposed that the Southern Hemisphere Mechanism (SHM), connecting the phase transition of SAM and SIOD, could induce the early onset of IOD events in the absence of ENSO. However, the autumn pIOD, which accompanies the SIOD in the preceding boreal spring, is

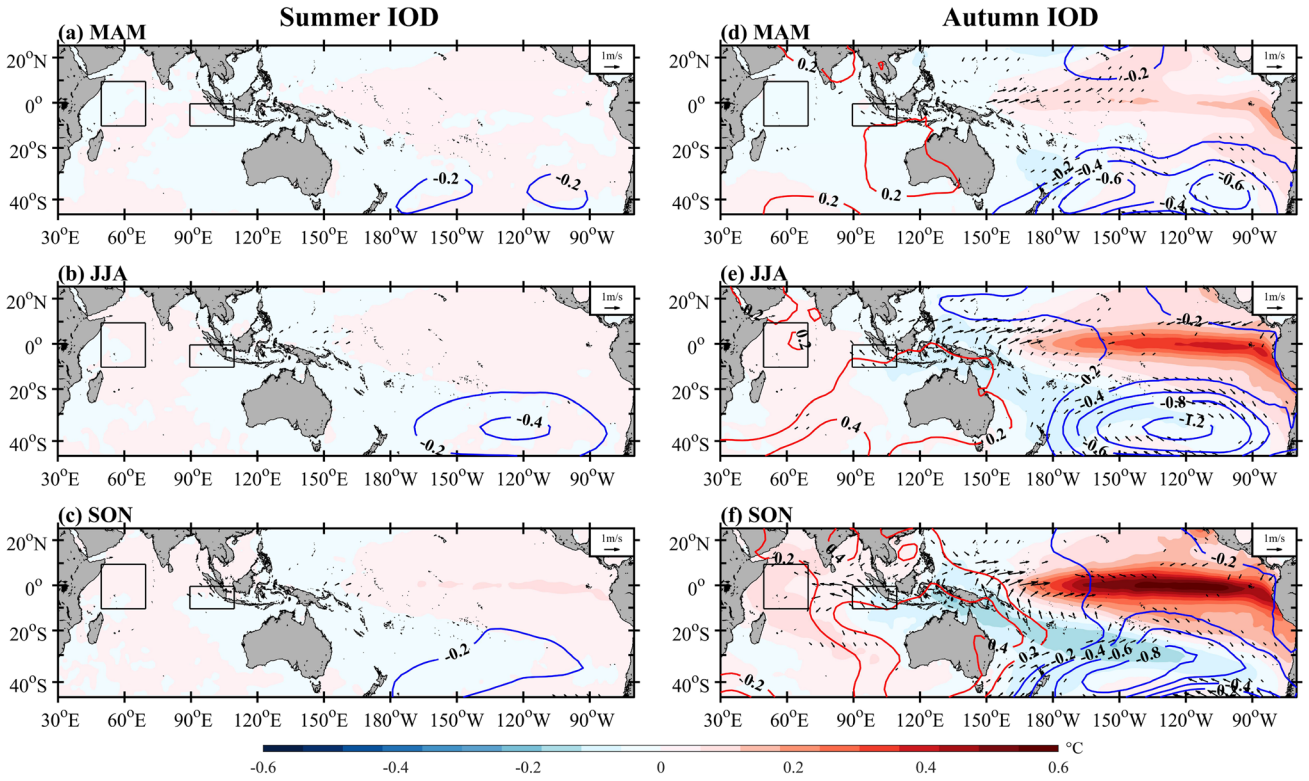

Fig. 10 Regression of SSTAs (shading, units: ℃), surface wind anomalies (vectors, units: m s^{-1}), and SLPA (contour, units: hPa) upon Niño 3.4 index for the summer IOD (**a**–**c**) and autumn IOD (**d**–**f**), from the developing spring to the succeeding autumn. Datasets for SST: HadISST and ERSST. Anomalies are standardized by the amplitude of ENSO before composite. Only wind vectors that exceed 0.1 m s^{-1} are shown

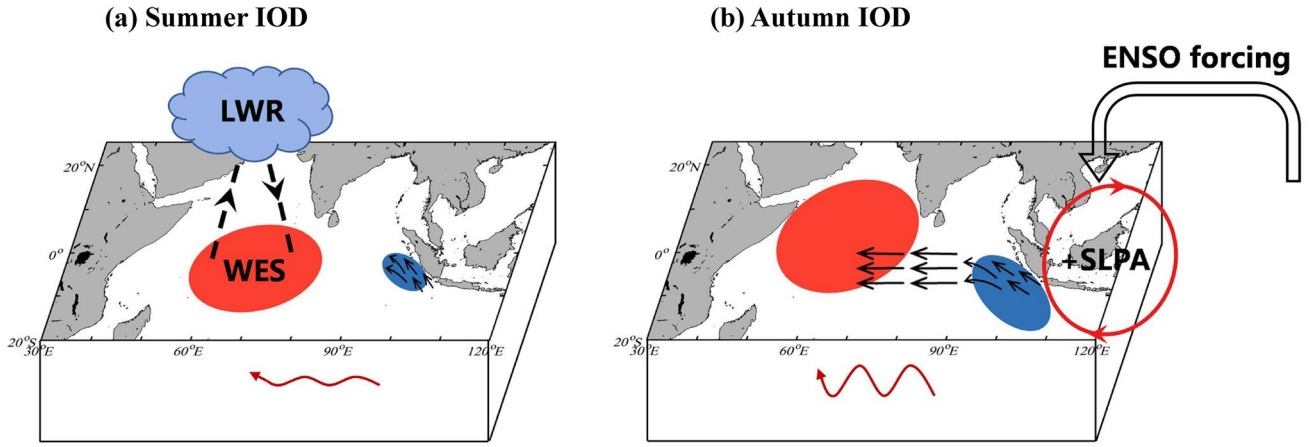

Fig. 11 Schematic diagram of the mechanisms for the development of (**a**) the summer IOD and (**b**) the autumn IOD. (**a**) WES and LWR respectively indicate wind-evaporation-SST feedback and longwave radiation reflected, contributing to the SST warming in the WIO of the summer IOD. (**b**) As a response to El Niño, positive SLPA with anticyclonic atmospheric circulation is favorable for the intensification of easterly wind anomalies, therefore dominates the formation of the western and eastern poles via oceanic downwelling Rossby waves and Bjerknes feedback. The black vectors denote the easterly wind anomalies. The red curve denotes the Rossby waves

shown to concurrently occur with El Niño events (Fig. 2f). Therefore, further investigation is needed to understand how the mid-high latitude climate signals modulate the tropical ocean–atmosphere couplings accounting for the two types of IOD presented in this study.

Author contributions All authors contributed to the study's conception and design. WZ, CQ and YT conceived the idea of the study. Material preparation, data collection, and analysis were performed by YT, WZ, and CQ. The first draft of the manuscript was written by YT, and all authors commented on previous versions of the manuscript. WZ and CQ supervised this study. All authors read and approved the final manuscript.

Funding This study was supported by the National Natural Science Foundation of China (Grant Nos. 92158204 and 42105052), the National Key R&D Program of China (Grant No. 2020YFA0608803), and an Innovation Group Project of the Southern Marine Science and Engineering Guangdong Laboratory (Zhuhai).

Data availability The monthly HadISST1 datasets used during the current study are available at the https://www.metoffice.gov.uk/hadobs/hadisst/data/download.html. The ocean potential temperature, oceanic circulation data, total downward net surface heat flux, and SSH datasets from GODAS are available at the https://www.psl.noaa.gov/data/gridded/data.godas.html. The surface wind and SLP datasets from NCEP-NCAR are available at the https://psl.noaa.gov/data/gridded/data.ncep.reanalysis.html. The OLR datasets from NOAA are available at https://www.ncei.noaa.gov/data/outgoing-longwave-radiation-monthly/access/. The latent heat flux, sensible heat flux, longwave radiation, and shortwave radiation are available at the https://oaflux.whoi.edu/. The ocean potential temperature and oceanic circulation data from SODA 3.3.1 and ORAS5 are both available at http://apdrc.soest.hawaii.edu/data/data.php. The ERSST dataset is available at https://www.ncei.noaa.gov/pub/data/cmb/ersst/v5/netcdf/. The ERA5 dataset is available at https://cds.climate.copernicus.eu/.

Declarations

Conflict of interest The authors have no relevant financial or non-financial interests to disclose.

References

Annamalai H, Murtugudde R, Potemra J et al (2003) Coupled dynamics over the Indian ocean: spring initiation of the zonal mode. Deep sea res part II. Top Stud Oceanogr 50:2305–2330. https://doi.org/10.1016/S0967-0645(03)00058-4

Ashok K, Guan ZY, Yamagata T (2001) Impact of the Indian Ocean Dipole on the relationship between the Indian monsoon rainfall and ENSO. Geophys Res Lett 28:4499–4502. https://doi.org/10.1029/2001GL013294

Ashok K, Guan ZY, Yamagata T (2003) A look at the relationship between the ENSO and the Indian Ocean dipole. J Meteorol Soc Jpn Ser II 81:41–56. https://doi.org/10.2151/jmsj.81.41

Behera SK, Yamagata T (2001) Subtropical SST dipole events in the southern Indian Ocean. Geophys Res Lett 28:327–330. https://doi.org/10.1029/2000GL011451

Behera SK, Luo JJ, Masson S et al (2006) A CGCM study on the interaction between IOD and ENSO. J Clim 19:1688–1705. https://doi.org/10.1175/JCLI3797.1

Behringer DW, Ji M, Leetmaa A (1998) An improved coupled model for ENSO prediction and implications for ocean initialization. Part I: the ocean data assimilation system. Mon Weather Rev 126:1013–1021. https://doi.org/10.1175/1520-0493(1998)126%3c1013:AICMFE%3e2.0.CO;2

Bjerknes J (1969) Atmospheric teleconnections from the equatorial pacific. Mon Weather Rev 97:163–172. https://doi.org/10.1175/1520-0493(1969)097%3c0163:ATFTEP%3e2.3.CO;2

Cai W, Sullivan A, Cowan T (2011a) Interactions of ENSO, the IOD, and the SAM in CMIP3 models. J Clim 24:1688–1704. https://doi.org/10.1175/2010JCLI3744.1

Cai W, van Rensch P, Cowan T, Hendon HH (2011b) Teleconnection pathways of ENSO and the IOD and the mechanisms for impacts on Australian rainfall. J Clim 24:3910–3923. https://doi.org/10.1175/2011JCLI4129.1

Cai W, Yang K, Wu L et al (2021) Opposite response of strong and moderate positive Indian Ocean dipole to global warming. Nat Clim Change 11:27–32. https://doi.org/10.1038/s41558-020-00943-1

Carton JA, Chepurin GA, Chen L (2018) SODA3: a new ocean climate reanalysis. J Clim 31:6967–6983. https://doi.org/10.1175/JCLI-D-18-0149.1

Chen G, Han W, Li Y, Wang D (2016) Interannual variability of equatorial eastern Indian ocean upwelling: local versus remote forcing*. J Phys Oceanogr 46:789–807. https://doi.org/10.1175/JPO-D-15-0117.1

Chen P, Sun B, Wang H, Zhu B (2021) Possible impacts of december laptev sea ice on Indian ocean dipole conditions during spring. J Clim 34:6927–6943. https://doi.org/10.1175/JCLI-D-20-0980.1

Dong S, Gille ST, Sprintall J (2007) An assessment of the southern ocean mixed layer heat budget. J Clim 20:4425–4442. https://doi.org/10.1175/JCLI4259.1

Drbohlav H-KL, Gualdi S, Navarra A (2007) A diagnostic study of the indian ocean dipole mode in El Niño and non–El Niño years. J Clim 20:2961–2977. https://doi.org/10.1175/JCLI4153.1

Du Y (2005) Seasonal heat budget in the mixed layer of the southeastern tropical Indian Ocean in a high-resolution ocean general circulation model. J Geophys Res 110:C04012. https://doi.org/10.1029/2004JC002845

Du Y, Cai W, Wu Y (2013) A new type of the indian ocean dipole since the mid-1970s. J Clim 26:959–972. https://doi.org/10.1175/JCLI-D-12-00047.1

Du Y, Zhang Y, Zhang L-Y et al (2020) Thermocline warming induced extreme Indian ocean dipole in 2019. Geophys Res Lett 47:e202. https://doi.org/10.1029/2020GL090079

Du Y, Wang F, Wang T et al (2023) Multi-scale ocean dynamical processes in the Indo-Pacific Convergence Zone and their climatic and ecological effects. Earth-Sci Rev 237:104313. https://doi.org/10.1016/j.earscirev.2023.104313

Effy JB, Francis PA, Ramakrishna SSVS, Mukherjee A (2020) Anomalous warming of the western equatorial Indian Ocean in 2007: role of ocean dynamics. Ocean Model 147:101542. https://doi.org/10.1016/j.ocemod.2019.101542

Endo S, Tozuka T (2016) Two flavors of the Indian ocean dipole. Clim Dyn 46:3371–3385. https://doi.org/10.1007/s00382-015-2773-0

Fan L, Liu Q, Wang C, Guo F (2017) Indian ocean dipole modes associated with different types of ENSO development. J Clim 30:2233–2249. https://doi.org/10.1175/JCLI-D-16-0426.1

Feng J, Hu D, Yu L (2014) How does the Indian Ocean subtropical dipole trigger the tropical Indian Ocean dipole via the Mascarene

high? Acta Oceanol Sin 33:64–76. https://doi.org/10.1007/s13131-014-0425-6
Fischer AS, Terray P, Guilyardi E et al (2005) Two independent triggers for the Indian ocean dipole/zonal mode in a coupled GCM. J Clim 18:3428–3449. https://doi.org/10.1175/JCLI3478.1
Francis PA, Gadgil S, Vinayachandran PN (2007) Triggering of the positive Indian Ocean dipole events by severe cyclones over the Bay of Bengal. Tellus Dyn Meteorol Oceanogr 59:461–475. https://doi.org/10.1111/j.1600-0870.2007.00254.x
Guo F, Liu Q, Sun S, Yang J (2015) Three types of Indian ocean dipoles. J Clim 28:3073–3092. https://doi.org/10.1175/JCLI-D-14-00507.1
Halkides DJ, Lee T (2009) Mechanisms controlling seasonal-to-interannual mixed layer temperature variability in the southeastern tropical Indian Ocean. J Geophys Res Oceans 114:C02012. https://doi.org/10.1029/2008JC004949
He B, Liu Y, Wu G et al (2019) The role of air–sea interactions in regulating the thermal effect of the Tibetan-Iranian Plateau on the Asian summer monsoon. Clim Dyn 52:4227–4245. https://doi.org/10.1007/s00382-018-4377-y
Hersbach H, Bell B, Berrisford P et al (2020) The ERA5 global reanalysis. Q J R Meteorol Soc 146:1999–2049. https://doi.org/10.1002/qj.3803
Hong C-C, Li T, Ho L, Kug J-S (2008a) Asymmetry of the Indian Ocean dipole Part I: observational analysis. J Clim 21:4834–4848. https://doi.org/10.1175/2008JCLI2222.1
Hong C-C, Li T, Luo J-J (2008b) Asymmetry of the Indian ocean dipole. Part II: model diagnosis. J Clim 21:4849–4858. https://doi.org/10.1175/2008JCLI2223.1
Hong C-C, Lu M-M, Kanamitsu M (2008c) Temporal and spatial characteristics of positive and negative Indian Ocean dipole with and without ENSO. J Geophys Res-Atmos 113:D08107. https://doi.org/10.1029/2007JD009151
Huang B, Thorne PW, Banzon VF et al (2017) Extended reconstructed sea surface temperature, version 5 (ERSSTv5): upgrades, validations, and intercomparisons. J Clim 30:8179–8205. https://doi.org/10.1175/JCLI-D-16-0836.1
Huang K, Wang D, Feng M et al (2020) Baroclinic characteristics and energetics of annual Rossby waves in the southern tropical Indian ocean. J Phys Oceanogr 50:2591–2607. https://doi.org/10.1175/JPO-D-19-0294.1
Huang B, Su T, Qu S et al (2021) Strengthened relationship between tropical indian ocean dipole and subtropical indian ocean dipole after the late 2000s. Geophys Res Lett 48:e2021. https://doi.org/10.1029/2021GL094835
Jiang J, Liu Y (2022) Impact of march north Atlantic oscillation on Indian ocean dipole: role of air–sea interaction over the western north pacific. Clim Dyn. https://doi.org/10.1007/s00382-022-06583-9
Jiang J, Liu Y, Mao J et al (2022) Three types of positive Indian ocean dipoles and their relationships with the south Asian summer monsoon. J Clim 35:405–424. https://doi.org/10.1175/JCLI-D-21-0089.1
Kalnay E, Kanamitsu M, Kistler R et al (1996) The NCEP/NCAR 40-year reanalysis project. Bull Am Meteorol Soc 77:437–472. https://doi.org/10.1175/1520-0477(1996)077%3c0437:TNYRP%3e2.0.CO;2
Lau NC, Nath MJ (2004) Coupled GCM simulation of atmosphere-ocean variability associated with zonally asymmetric SST changes in the tropical Indian Ocean. J Clim 17:245–265. https://doi.org/10.1175/1520-0442(2004)017%3c0245:CGSOAV%3e2.0.CO;2
Li CY, Mu MQ (2001) The influence of the Indian Ocean dipole on atmospheric circulation and climate. Adv Atmospheric Sci 18:831–843. https://doi.org/10.1007/BF03403506
Liebmann B, Smith CA (1996) Description of a complete (interpolated) outgoing longwave radiation dataset. Bull Am Meteorol Soc 77:1275–1277
Ling F, Luo J-J, Li Y et al (2022) Multi-task machine learning improves multi-seasonal prediction of the Indian Ocean Dipole. Nat Commun 13:7681. https://doi.org/10.1038/s41467-022-35412-0
Liu H, Tang Y, Chen D, Lian T (2017) Predictability of the Indian Ocean dipole in the coupled models. Clim Dyn 48:2005–2024. https://doi.org/10.1007/s00382-016-3187-3
Lu B, Ren H-L (2020) What caused the extreme Indian ocean dipole event in 2019? Geophys Res Lett 47:e2020. https://doi.org/10.1029/2020GL087768
Luo J-J, Behera S, Masumoto Y et al (2008) Successful prediction of the consecutive IOD in 2006 and 2007. Geophys Res Lett 35:L14S02. https://doi.org/10.1029/2007GL032793
Luo J-J, Zhang R, Behera SK et al (2010) Interaction between El Niño and Extreme Indian Ocean Dipole. J Clim 23:726–742. https://doi.org/10.1175/2009JCLI3104.1
Murtugudde R, Busalacchi AJ (1999) Interannual variability of the dynamics and thermodynamics of the tropical Indian ocean. J Clim 12:2300–2326. https://doi.org/10.1175/1520-0442(1999)012%3c2300:IVOTDA%3e2.0.CO;2
Ng B, Cai W, Walsh K, Santoso A (2015) Nonlinear processes reinforce extreme Indian ocean dipole events. Sci Rep 5:11697. https://doi.org/10.1038/srep11697
Paulson CA, Simpson JJ (1977) Irradiance measurements in the upper ocean. J Phys Oceanogr 7:952–956. https://doi.org/10.1175/1520-0485(1977)007%3c0952:IMITUO%3e2.0.CO;2
Rao SA, Behera SK (2005) Subsurface influence on SST in the tropical Indian ocean: structure and interannual variability. Dyn Atmos Oceans 39:103–135. https://doi.org/10.1016/j.dynatmoce.2004.10.014
Rayner NA (2003) Global analyses of sea surface temperature, sea ice, and night marine air temperature since the late nineteenth century. J Geophys Res 108:4407. https://doi.org/10.1029/2002JD002670
Rogers JC, van Loon H (1982) Spatial variability of sea level pressure and 500 mb height anomalies over the southern hemisphere. Mon Weather Rev 110:1375–1392. https://doi.org/10.1175/1520-0493(1982)110%3c1375:SVOSLP%3e2.0.CO;2
Roxy M, Gualdi S, Drbohlav H-KL, Navarra A (2011) Seasonality in the relationship between El Nino and Indian Ocean dipole. Clim Dyn 37:221–236. https://doi.org/10.1007/s00382-010-0876-1
Saji NH, Yamagata T (2003) Possible impacts of Indian ocean dipole mode events on global climate. Clim Res 25:151–169. https://doi.org/10.3354/cr025151
Saji NH, Goswami BN, Vinayachandran PN, Yamagata T (1999) A dipole mode in the tropical Indian Ocean. Nature 401:360–363. https://doi.org/10.1038/43854
Santoso A, Sen Gupta A, England MH (2010) Genesis of Indian ocean mixed layer temperature anomalies: a heat budget analysis. J Clim 23:5375–5403. https://doi.org/10.1175/2010JCLI3072.1
Schott FA, Xie S-P, McCreary JP (2009) Indian ocean circulation and climate variability. Rev Geophys 47:1002. https://doi.org/10.1029/2007RG000245
Song G, Ren R (2022) How can the positive Indian ocean dipole events co-occur with La Niña? Int J Climatol 42:8724–8737. https://doi.org/10.1002/joc.7766
Song Q, Vecchi GA, Rosati AJ (2007) The role of the Indonesian throughflow in the Indo-Pacific climate variability in the GFDL coupled climate model. J Clim 20:2434–2451. https://doi.org/10.1175/JCLI4133.1

Stuecker MF, Timmermann A, Jin F-F et al (2017) Revisiting ENSO/Indian Ocean dipole phase relationships. Geophys Res Lett 44:2481–2492. https://doi.org/10.1002/2016GL072308

Sun S, Fang Y, Tana LB (2014) Dynamical mechanisms for asymmetric SSTA patterns associated with some Indian Ocean Dipoles. J Geophys Res-Oceans 119:3076–3097. https://doi.org/10.1002/2013JC009651

Sun S, Lan J, Fang Y et al (2015) A triggering mechanism for the Indian ocean dipoles independent of ENSO. J Clim 28:5063–5076. https://doi.org/10.1175/JCLI-D-14-00580.1

Terray P, Chauvin F, Douville H (2007) Impact of southeast Indian Ocean sea surface temperature anomalies on monsoon-ENSO-dipole variability in a coupled ocean–atmosphere model. Clim Dyn 28:553–580. https://doi.org/10.1007/s00382-006-0192-y

Thompson DWJ, Wallace JM (2000) Annular modes in the extratropical circulation Part i: month-to-month variability. J Clim 13:1000–1016. https://doi.org/10.1175/1520-0442(2000)013%3c1000:AMITEC%3e2.0.CO;2

Tozuka T, Luo J-J, Masson S, Yamagata T (2007) Decadal modulations of the Indian ocean dipole in the SINTEX-F1 coupled GCM. J Clim 20:2881–2894. https://doi.org/10.1175/JCLI4168.1

Vijith V, Vinayachandran PN, Webber BGM et al (2020) Closing the sea surface mixed layer temperature budget from in situ observations alone: operation advection during BoBBLE. Sci Rep 10:7062. https://doi.org/10.1038/s41598-020-63320-0

Wang X, Wang C (2014) Different impacts of various El Niño events on the Indian Ocean Dipole. Clim Dyn 42:991–1005. https://doi.org/10.1007/s00382-013-1711-2

Wang H, Murtugudde R, Kumar A (2016) Evolution of Indian Ocean dipole and its forcing mechanisms in the absence of ENSO. Clim Dyn 47:2481–2500. https://doi.org/10.1007/s00382-016-2977-y

Wang Y, Li J, Zhang Y et al (2019) Atmospheric energetics over the tropical Indian Ocean during Indian Ocean dipole events. Clim Dyn 52:6243–6256. https://doi.org/10.1007/s00382-018-4510-y

Webster PJ, Moore AM, Loschnigg JP, Leben RR (1999) Coupled ocean-atmosphere dynamics in the Indian Ocean during 1997–98. Nature 401:356–360. https://doi.org/10.1038/43848

Xie S-P, Philander SGH (1994) A coupled ocean-atmosphere model of relevance to the ITCZ in the eastern Pacific. Tellus A 46:340–350. https://doi.org/10.1034/j.1600-0870.1994.t01-1-00001.x

Xie S-P, Annamalai H, Schott FA, McCreary JP (2002) Structure and mechanisms of south Indian ocean climate variability*. J Clim 15:864–878. https://doi.org/10.1175/1520-0442(2002)015%3c0864:SAMOSI%3e2.0.CO;2

Xie S-P, Hu K, Hafner J et al (2009) Indian ocean capacitor effect on Indo-western pacific climate during the summer following El Nino. J Clim 22:730–747. https://doi.org/10.1175/2008JCLI2544.1

Xie S-P, Kosaka Y, Du Y et al (2016) Indo-western Pacific ocean capacitor and coherent climate anomalies in post-ENSO summer: a review. Adv Atmos Sci 33:411–432. https://doi.org/10.1007/s00376-015-5192-6

Yang Y, Xie S-P, Wu L et al (2015) Seasonality and predictability of the Indian ocean dipole mode: ENSO forcing and internal variability. J Clim 28:8021–8036. https://doi.org/10.1175/JCLI-D-15-0078.1

Yu LS, Rienecker MM (1999) Mechanisms for the Indian Ocean warming during the 1997–98 El Nino. Geophys Res Lett 26:735–738. https://doi.org/10.1029/1999GL900072

Yu L, Weller RA (2007) Objectively analyzed air-sea heat fluxes for the global ice-free oceans (1981–2005). Bull Am Meteorol Soc 88:527–540. https://doi.org/10.1175/BAMS-88-4-527

Zhang Y, Du Y (2022) Oceanic Rossby waves induced two types of ocean-atmosphere response and opposite Indian ocean dipole phases. J Clim 35:3927–3945. https://doi.org/10.1175/JCLI-D-21-0426.1

Zhang W, Wang Y, Jin F-F et al (2015) Impact of different El Niño types on the El Niño/IOD relationship. Geophys Res Lett 42:8570–8576. https://doi.org/10.1002/2015GL065703

Zhang L, Du Y, Cai W (2018) A spurious positive Indian ocean dipole in 2017. Sci Bull 63:1170–1172. https://doi.org/10.1016/j.scib.2018.08.001

Zhang Y, Li J, Xue J et al (2019) The relative roles of the South China Sea summer monsoon and ENSO in the Indian Ocean dipole development. Clim Dyn 53:6665–6680. https://doi.org/10.1007/s00382-019-04953-4

Zhang L, Du Y, Cai W et al (2020) Triggering the Indian ocean dipole from the Southern Hemisphere. Geophys Res Lett 47:e2020. https://doi.org/10.1029/2020GL088648

Zhang S, Wang H, Jiang H, Ma W (2021) Studies of the seasonal prediction of heavy late spring rainfall over southeastern China. Clim Dyn 57:1919–1931. https://doi.org/10.1007/s00382-021-05786-w

Zhang G, Wang X, Xie Q et al (2022a) Strengthening impacts of spring sea surface temperature in the north tropical Atlantic on Indian Ocean dipole after the mid-1980s. Clim Dyn 59:185–200. https://doi.org/10.1007/s00382-021-06128-6

Zhang M, Jin D, Wang X et al (2022b) Seasonal transition of precedent Indian Ocean basin mode and subsequent Indian Ocean Dipole without El Niño-Southern Oscillation impact. Int J Climatol 42:9023–9031. https://doi.org/10.1002/joc.7793

Zhong W, Wu Y, Yang S et al (2023) Heavy Southern China spring rainfall promoted by multi-year El Niño events. Geophys Res Lett 50:e2022. https://doi.org/10.1029/2022GL102346

Zuo H, Balmaseda MA, Tietsche S et al (2019) The ECMWF operational ensemble reanalysis–analysis system for ocean and sea ice: a description of the system and assessment. Ocean Sci 15:779–808. https://doi.org/10.5194/os-15-779-2019